# Meshless Numerical Solution of Boundary Integral Equations based on Non Uniform Rational Basis-Splines

**Vincenzo Marchese and Umberto Iemma**

*Department of Engineering, Roma Tre University, via Vito Volterra, 62, Roma, Italy*

(Received 15 August 2013; accepted 11 December 2014

The paper deals with the use of Non Uniform Rational Basis-Splines (NURBS) for the global representation of domain geometry and unknown functions aimed at the numerical solution of Boundary Integral Equations (BIE). The use of a global NURBS function basis yields a meshless method which does not need the partition of the boundary into elements. The level of the accuracy in the representation of dependent and independent variables can be changed in each simulation, according to the problem requirements, thanks to the recursive definition of NURBS. The solving system of equations is assembled by means of the collocation of the integral equation onto the Greville abscissae in the NURBS parametric space. The unknowns are the locations of the control points in the vector space the unknown function belongs to. Preliminary numerical results have been obtained in potential aerodynamics and acoustic scattering. The numerical solution reveals a remarkable level of accuracy in all the test cases analyzed with a convergence rate always higher than the order of the NURBS adopted.

## 1. INTRODUCTION

In many fields of application, the Boundary Integral Equations (BIE) approach is a well established technique to address the solution of Boundary Value Problems (BVP). Using the BIE, it is possible to represent the unknown function at any location in the domain as a function of its Cauchy data set. This approach is more recently considered as standard in incompressible and compressible potential aerodynamics, structural elasticity, heat conduction, electromagnetism, acoustics, and aeroacoustics. The numerical solution typically relies on the Boundary Element Method (BEM), in all its variants and declinations. In classic BEM the boundary of the domain is partitioned into finite elements, where the dependent and independent variables are approximated using suitable local basis functions. The greatest advantage of the numerical methods based on BIE resides in the reduction of the computational burden required for the numerical solution, due to the reduced dimensionality of the problem. Although this approach is usually convenient with respect to the so-called *field* methods, such as Finite Volumes Method (FV), Finite Difference Method (FDM), or Finite Element Method (FEM), in some specific application the number of boundary elements required to capture a specific feature of the phenomenon may become extremely high. This is the case, for example, for acoustic propagation and scattering problems, where the wave length of the perturbation at high frequencies can be orders of magnitude smaller than the characteristic length of the domain of interest, thus requiring a huge amount of boundary panels to correctly reproduce the scattering and interference effects. One of the possible approaches to mitigate this difficulty is improving the accuracy of the local representation of the variables using higher-order functions. This allows for the reduction of the number of elements needed to achieve the desired level of accuracy. In this respect, the literature available is very extensive, and an in-depth review is beyond the scope of the paper. Among others, it is worth mentioning the use of third order polynomials based on Overhauser[1,2] or Hermite[3,4] elements, recently coupled with Coons patches.[5] The typical limitation of all the approaches based on the local representation of the variables is the restriction of the resulting numerical formulation to a single order of accuracy, fixed by the order of the polynomial shape functions used. The possibility to overcome this limitation has already been investigated within the context of the finite element method[6] using an approach based on generalized Hermite polynomials. However, a similar attempt for the solution of BIE is still missing. This goal has been the driving motivation in the development of the method presented here. Indeed, using a global representation of the variables based on NURBS, the order of the basis functions can be improved when needed by the specific application in discussion. This is a consequence of the iterative definition of the NURBS, which makes possible the increase of the NURBS degree simply by changing an input parameter. The use of the NURBS for the representation of curves and surfaces is a common technique in the CAD community for the modeling of complex geometries with strict requirements of smoothness and continuity between patches.[7,8] Their use in the numerical solution of BIE is not new, although it is relatively recent. NURBS have been used to develop boundary element solutions of integral equations in elastostatics,[9] in radiation and diffraction problems,[10] and in potential aerodynamics.[11] As already mentioned, the peculiarity of the present method is in the use of the NURBS for the development of a global isogeometric approach aimed at the meshless numerical solution of the BVP. The control points used for the representation of the dependent variables are obtained through the *h*-refinement of the optimal NURBS

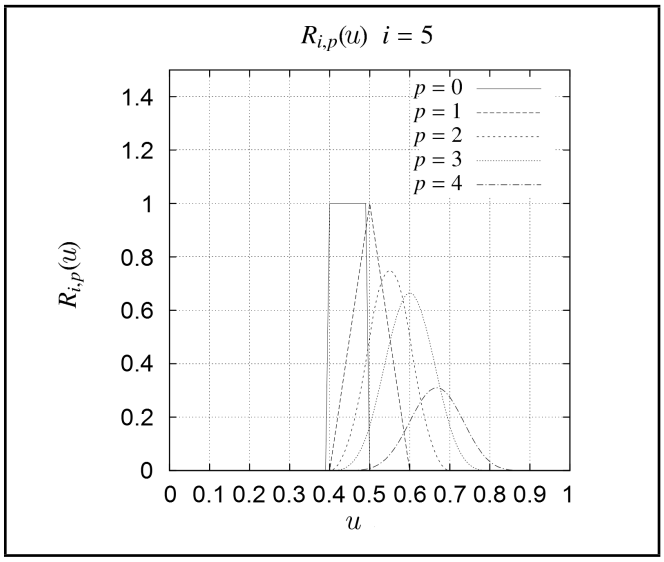


**Figure 1.** Function $R_{i,p}(u)$ for $u_i = 0.5$ and $0 \leq p \leq 5$.

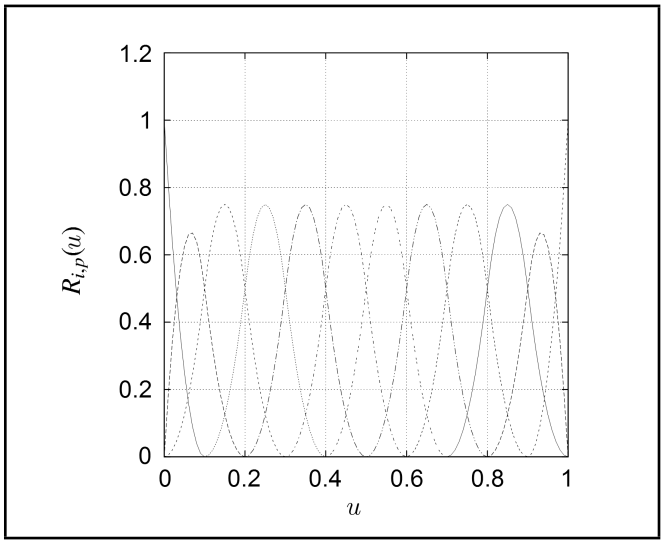


**Figure 2.** NURBS basis for $p = 2$.

representation of the geometry. The final system of equation is obtained by means of a collocation method based on the use of the Greville abscissae in the parametric space.

The paper is organized as follows: The global NURBS decomposition of a generic BIE formulation is presented in section 2, whereas the collocation method and the *h*-refinement technique are outlined in section 3. Section 4 reports the results of preliminary numerical simulations, and includes the analysis of the convergence of the solution as a function of the number of control points used. Appendix A is dedicated to some consideration about the integration strategy adopted to handle the singularity of the kernels.

## 2. NURBS REPRESENTATION OF BIE

Consider a physical phenomenon governed by the Laplacian of the function $\varphi(\boldsymbol{x})$, for $\boldsymbol{x} \in \Omega$. The BIE formulation of such a problem has the form

$$E(\boldsymbol{y})\,\varphi(\boldsymbol{y}) = \oint_\Gamma \left( G \frac{\partial \varphi}{\partial n} - \frac{\partial G}{\partial n}\,\varphi \right) \mathrm{d}\Gamma(\boldsymbol{x}); \qquad (1)$$

where $G(\boldsymbol{x}, \boldsymbol{y})$ is the fundamental solution of the governing partial differential equation, $\Gamma$ is the boundary of the domain $\Omega$, $\boldsymbol{x} \in \Gamma$, $\boldsymbol{y} \in \overline{\Omega} = \Omega \cup \Gamma$, and $\partial\varphi/\partial n = \nabla\varphi \cdot \boldsymbol{n}$, being $\boldsymbol{n}$ the unit normal to $\Gamma$ pointing into $\Omega$. The value of the domain function $E(\boldsymbol{y})$ is $1, 1/2, 0$ for $\boldsymbol{y} \in \Omega$, $\boldsymbol{y} \in \Gamma$ or $\boldsymbol{y} \notin \overline{\Omega}$, respectively (see appendix A). When the Cauchy data of the problem are known, Eq. 1 is an integral representation of $\varphi(\boldsymbol{y})$ for $\boldsymbol{y} \in \Omega$. On the other hand, when only part of the Cauchy set is known from the boundary conditions, Eq. (1) can be used as an integral equation for the unknown corresponding to the missing part of the boundary data. If, for example, the differential problem exhibits Neumann boundary conditions, then Eq. (1) can be written as

$$E(\boldsymbol{y})\,\varphi(\boldsymbol{y}) = \oint_\Gamma \mathcal{K}(\boldsymbol{y}, \boldsymbol{x})\;\varphi(\boldsymbol{x})\mathrm{d}\Gamma(\boldsymbol{x}) + b(\boldsymbol{y}); \qquad (2)$$

which is a Fredholm integral equation of the second kind in the unknown $\varphi(\boldsymbol{x})$, with kernel $\mathcal{K}(\boldsymbol{y}, \boldsymbol{x}) = -\nabla G(\boldsymbol{y}, \boldsymbol{x}) \cdot \boldsymbol{n}$, and where

$$b(\boldsymbol{y}) = \oint_\Gamma G(\boldsymbol{y}, \boldsymbol{x})\;\frac{\partial \varphi}{\partial n}\mathrm{d}\Gamma(\boldsymbol{x}) \qquad (3)$$

is known.[12,13] The BIE so obtained can be solved numerically through the BEM, by partitioning the boundary $\Gamma$ into $M$ elements and introducing a local representation of the dependent and independent variables using an appropriate function basis. In the present work, the numerical solution of Eq. (2) is obtained using a global, isogeometric NURBS decomposition. The general form of a NURBS curve is

$$f(u) = \frac{\sum_{i=1}^{N} N_{i,p}(u) W_i q_i}{\sum_{i=1}^{N} N_{i,p}(u) W_i}, \qquad u \in [0,1]; \qquad (4)$$

where the rational basis functions of order $p$, $N_{i,p}(u)$ are defined in a recursive way as

$$N_{i,p}(u) = \frac{u - u_i}{u_{i+p} - u_i} N_{i,p-1}(u) + \frac{u_{i+p+1} - u}{u_{i+p+1} - u_{i+1}} N_{i+1,p-1}(u); \qquad (5)$$

with

$$N_{i,0}(u) = \begin{cases} 1 & \text{if} \quad u_i \leq u < u_{i+1} \\ 0 & \text{otherwise} \end{cases} . \qquad (6)$$

The points $q_i$ are called *control points* and the quantities $W_i$ are the weights of the NURBS. The set of abscissae $u_i$ needed to fully define the basis functions forms the *knot vector*. If the knot vector has $p + 1$ elements repeated at its beginning and at its end, it is called an *open* knot vector. In general, for a NURBS curve the following two properties hold:

1. if a knot $u_i$ is repeated $k$ times, the continuity of the curve at that point is $C^{p-k}$.
2. if the curve is $C^0$ at a point, the control point belongs to the curve.

As a consequence, for a given open knot vector the resulting NURBS passes through the first and last control points. Equation (4) can be written as

$$f(u) = \sum_{i=1}^{N} R_{i,p}(u) q_i, \qquad u \in [0,1]; \qquad (7)$$

with

$$R_{i,p}(u) = \frac{N_{i,p}(u)W_i}{\sum_{i=1}^{n} N_{i,p}(u)W_i}. \quad (8)$$

The function $R_{i,p}(u)$ for $u_i = 0.5$ and $0 \leq p \leq 5$ is depicted in Fig. 1, whereas Fig. 2 shows the complete basis in $u \in [0, 1]$, for $p = 2$.

On the basis of Eqs. (4) to (8) the NURBS representation of $\varphi$ has the form

$$\varphi(u) = \sum_{i=1}^{N} R_{i,p}(u)q_i; \quad (9)$$

with coefficients $q_i$ and basis functions as reported in Eq. (8). Applying Eq. (9) to the RHS of Eq. (2), and limiting, for the sake of simplicity, the notation to the two-dimensional case, we obtain

$$E(\boldsymbol{y})\varphi(\boldsymbol{y}) = b(\boldsymbol{y}) - \sum_{i=1}^{N} q_i \oint_{\Gamma} \frac{\partial G(u, \boldsymbol{y})}{\partial n} R_{i,p}(u)J(u)du; \quad (10)$$

where $J(u)$ is the Jacobian of the transformation from the physical space coordinate $\boldsymbol{x}$ to the NURBS parametric space one $u$. It is worth noting that the integrals in Eq. (10) span the whole boundary. Indeed, the use of the global NURBS representation makes the concept of surface elements no longer required for the numerical solution of Eq. (10) and thus the partition of $\Gamma$ is not strictly needed. On the other hand, the integrals in Eq. (10) must be accurately evaluated and, unless we have an analytical solution for them (and this could happen for very simple geometries and/or boundary conditions), a suitable numerical integration strategy must be identified. To this aim, a possible solution for complex geometries and/or boundary conditions could be the partition of the boundary into macro patches on which suitable quadrature formulas can be easily applied. However, it is important to notice that this partitioning, if needed, would have nothing to do with the number of unknowns of the solving linear system, but only with the proper evaluation of the integrals in Eq. (10). In appendix A the effects of the partition of $\Gamma$ on the convergence of the integrals in Eq. (10) is analyzed for two different geometries.

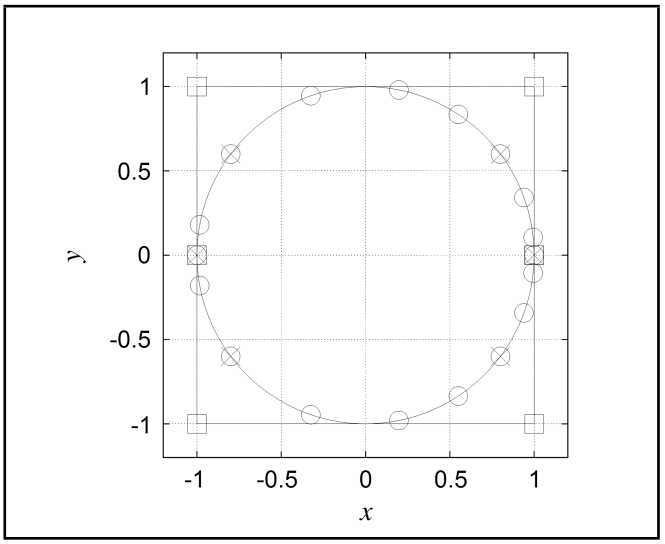


**Figure 3.** NURBS Circle, (□) control points, (×) Greville's abscissae in the physical space, (○) refined Greville's abscissae in the physical space.

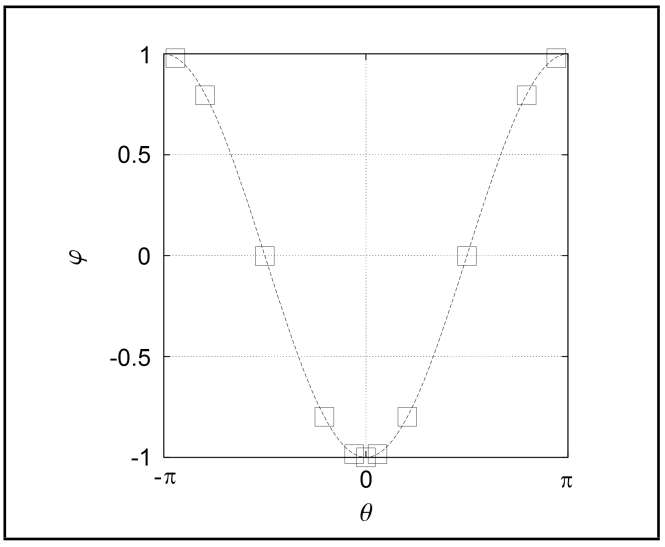


**Figure 4.** Velocity potential $\varphi$ for a uniform flow $U_\infty$ in $x$-direction. $(-)$ Analytical solution, (□) BIE-NURBS, $p = 3$.

## 3. THE NUMERICAL SOLUTION

The numerical solution of Eq. (10) can be obtained using the collocation method, with collocation points lying on the boundary $\Gamma$. To this aim, it is necessary to identify a set of collocation points $\boldsymbol{y}_k \in \Gamma$. In the present approach, this requires the identification of a set of abscissae $u_k$ in the NURBS parametric space corresponding to points on $\Gamma$ in the physical space through the relationship

$$\boldsymbol{y}(u_k) = \sum_{i=1}^{N} R_{i,p}(u_k)\boldsymbol{\eta}_i; \quad (11)$$

where $n$ is the number of the control points $\boldsymbol{\eta}_i$ used to build the NURBS reproducing the geometry of $\Gamma$. To ensure that $\boldsymbol{y}(u_k)$ is located on the boundary, the abscissa $u_k$ must be chosen according to the Greville distribution[9,14]

$$u_k^{'} = \frac{u_{i+1} + u_{i+2} + \ldots + u_{i+p}}{p}, \quad i = 1, \ldots, n-1. \quad (12)$$

The abscissae $u_k^{'}$ satisfying Eq. (12) correspond to points in the physical space such that $\boldsymbol{y}(u^{'}) \in \Gamma$ (see Fig. 3). A key aspect in the numerical evaluation of the integrals in Eq. (10) is the management of the singularities of the kernels arising from the collocation of the observation point $\boldsymbol{y}$ on the boundary. In this respect, the meshless approach presents a significant advantage with respect to the classic BEM, as the integration is now extended to the whole boundary or, for complex geometries, to a part of it significantly larger than a single boundary element. As a consequence, the verification for singularity occurrence, which is not a straightforward task with NURBS, is less critical, or even not required at all, thus simplifying the numerical integration procedure. The asymptotic behavior of the integral appearing in Eq. (2) is briefly explained in appendix A for the sake of clarity and completeness of the paper. Once that the location of the collocation points is fixed using the Greville abscissae we can apply the same decomposition given in Eq. (9)

to the left hand side of Eq. (10). For $\boldsymbol{y} \in \Gamma$ we obtain

$$\frac{1}{2}\mathsf{R}\,\mathsf{q} = \mathsf{b} - \mathsf{C}\,\mathsf{q}; \tag{13}$$

where the elements of $\mathsf{b}$ and $\mathsf{C}$ have the form

$$b_j = \oint_\Gamma G(\boldsymbol{x}, \boldsymbol{y}_j)\frac{\partial \varphi}{\partial n} d\Gamma,\ C_{ij} = \oint_\Gamma \frac{\partial G(u, \boldsymbol{y}_j)}{\partial n} R_{i,p}(u) J(u) du; \tag{14}$$

where $u \in [0, 1]$. The entries of the $N \times N$ matrix $\mathsf{R}$ have the form $\mathsf{R}_{ij} = R_{i,p}(u_j^{'})$. The final form of the linear system is $(0.5\,\mathsf{R} + \mathsf{C})\ \mathsf{q} = \mathsf{b}$, which can be solved using the most appropriate solver.

## 3.1. Knots *h*-refinement

In the derivation performed so far we assumed, without loss of generality, unit weights in Eq. (8). This choice is certainly not optimal for the representation of complex functions, but is the only one possible to easily represent the unknowns. Indeed, for a generic function $\varphi$ could be possible, in principle, to identify an optimal set of weights and control points capable to achieve a high level of accuracy with a limited number of degrees of freedom. In real applications, this can easily be done to represent regular geometries (for example, simple geometries of the boundary $\Gamma$). On the contrary, in complex phenomena, the optimal representation of the unknown $\varphi$ could be not a simple task. As an example, consider a domain bounded a circle. It can be represented exactly with the six control points depicted by squares in Fig. 3, provided that the vectors of the corresponding weights and nodes are $\mathsf{W}_c^T = \{1\ 0.5\ 0.5\ 1\ 0.5\ 0.5\ 1\}$ and $\mathsf{u}_c^T = \{0\ 0\ 0\ 0.25\ 0.5\ 0.5\ 0.75\ 1\ 1\ 1\}$, respectively (see, *e.g.*, Piegl[8]). On the other hand, the physical phenomenon described by the function $\varphi$ can be extremely complex, even if the boundary of the domain is so simple. If, for example, we are dealing with the scattering of an acoustic wave impinging on the circle at medium-high frequencies, $\mathsf{W}_c$ and $\mathsf{u}_c$ are clearly not suitable to accurately reproduce the scattering pattern. In order to increase the number of collocation points for the numerical solution of the BIE, the *h*-refinement technique is used, starting from the NURBS optimal representation of $\Gamma$. With the *h*-refinement technique, the non-zero intervals between the components of the knot vector $\mathsf{u}_c$ are refined with equally spaced knots. The number of inserted knots does not need to be the same for each interval, and thus the NURBS representation can be enriched only where needed. These new knots become the control points of the representation of the unknown $\varphi$. The refinement obtained using an uneven distribution of knots in the different intervals is depicted in Fig. 3 ($\circ$), along with the original knot vector ($\times$).

## 4. RESULTS AND DISCUSSION

The method presented in the paper was first applied to simple problems, for which analytical solutions are available, in order to validate the accuracy of the numerical results and assess its convergence for an increasing NURBS order, $p$. The problems chosen for this assessment were the incompressible, two-dimensional potential flow around an impermeable circular cylinder, and the scattering of a planar wave impinging on a sound-hard cylindrical obstacle.

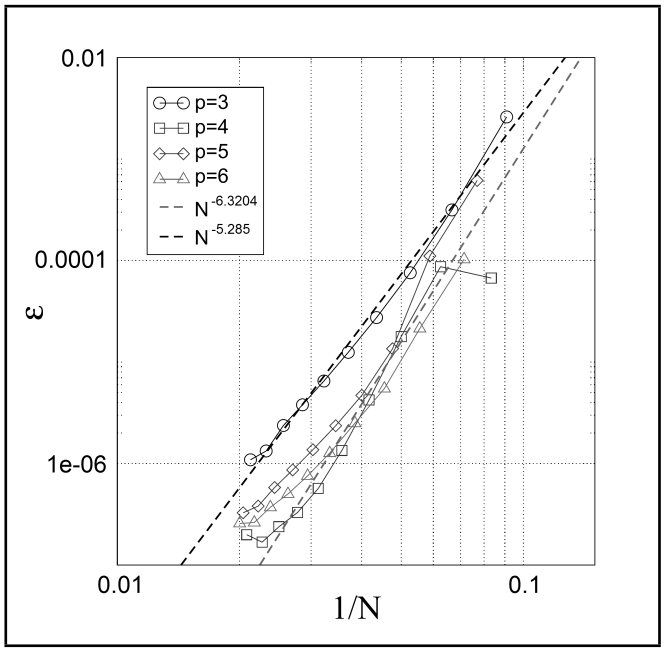


**Figure 5.** Convergence of $\epsilon$ for the solution of potential incompressible aerodynamics.

After this analysis, the method was tested on a boundary geometry of class $\mathcal{C}^0$, to demonstrate the capability of the method in the modelling of slope discontinuities of the boundary profile. Indeed, such a situation, which is very common in practical applications, could become critical for a global representation based on (at least) $\mathcal{C}^1$ continuous functions, so a careful treatment of the corner points is needed. Here, the two-dimensional scattering of a plane wave by a cylinder with a squared cross section is compared with an accurate numerical solution obtained with a widely assessed, highly accurate, commercial FEM code.

## 4.1. Assessment Against Analytical Solutions

As already mentioned, this section includes an analysis of the convergence of the numerical error with the order $p$ of the NURBS. This particular aspect deserves some preliminary clarification to put the obtained results in the proper perspective.

The method presented in this paper exhibits a $p-$type convergence to the asymptotic solution by increasing the order $p$ of the spline resulting from Eq. (9). On the other hand, the improvement of the solution for a given value of $p$ is obtained by refining the control points distribution (see section 3.1). On the other hand, the convergence obtained by increasing the number $N$ of control points cannot be exactly interpreted as an $h$-type convergence, because there is no mesh, and thus talking about mesh size $h$ would not apply. Nevertheless, the knots refinement improves the representation for a fixed order $p$. For these reasons, in the following the convergence diagrams are plotted as a function of the number of knots (*i.e.*, the number of unknowns) $N$ using $p$ as a parameter, similarly to what is done

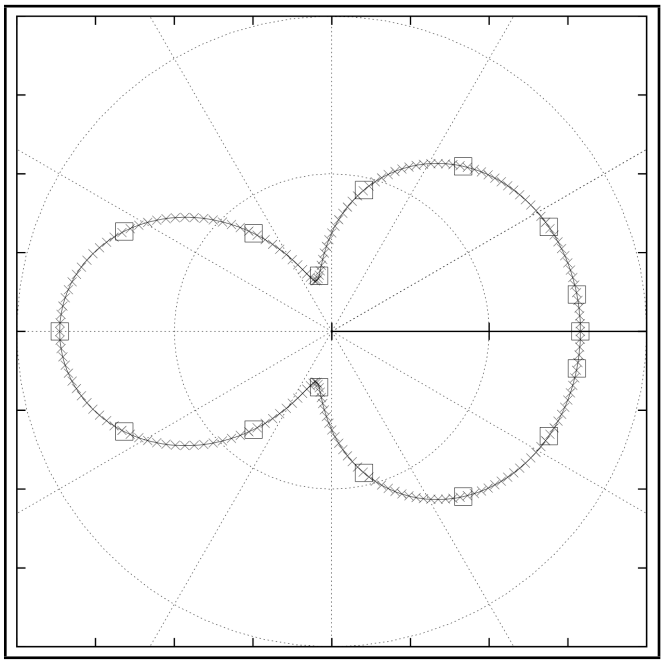

**Figure 6.** Scattering field on the cylinder, $f = 50Hz$. $(-)$ Analytical, $(\times)$ BIE-NURBS, $(\square)$ BIE-NURBS at Greville's abscissae.

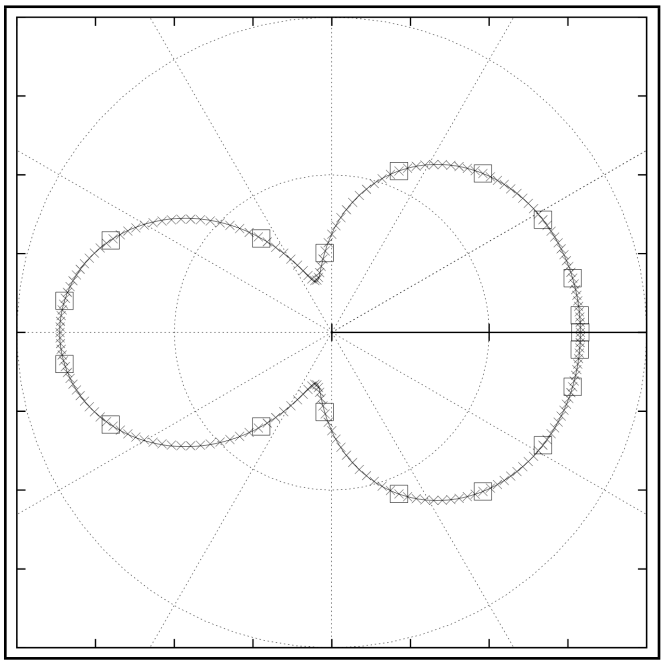

**Figure 7.** Effect of refinement at $f = 50Hz$. Scattering field, $(-)$ analytical, $(\times)$ BIE-NURBS, $(\square)$ BIE-NURBS at Greville's abscissae, $N = 20$, $p = 3$.

with $h$-type convergences. It is important to notice that the structure of the algorithm is such that for each value of $p$, the minimum number of unknowns is fixed (see Eq. (9)), and thus each convergence curve starts from a different $N$. To clarify, the convergence diagrams depict only the minimum and maximum convergence rates measured for the problem analysed, whereas the complete report of the rates observed is presented in Tables 1 and 2, including the minimum error.

For the sake of completeness, in appendix A the convergence of the numerical integration of the boundary integral in Eq. (10) is discussed for the case of a complex geometry. Indeed, the integrals resulting from the present global approach are defined over the entire boundary and for complex geometries the accuracy of their numerical evaluation can be improved by partitioning the domain into *macro-elements*. It must be stressed that this partition has nothing to do with the asymptotic behavior of the method, and is only intended for the accurate calculation of the matrix coefficients.

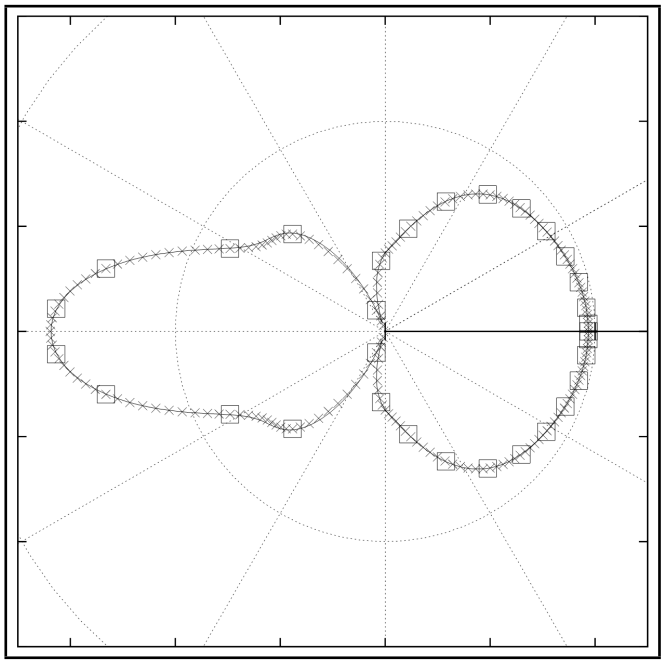

**Figure 8.** Scattering field at $f = 200Hz$, $(-)$ analytical, $(\times)$ BIE-NURBS, $(\square)$ BIE-NURBS at Greville's abscissae, $N = 32$, $p = 3$.

#### 4.1.1. Incompressible Potential Flow Around a Unit Circle

In the first application, the function $\varphi$ has the physical meaning of the velocity potential associated to the irrotational flow of an inviscid fluid. In such a flow $\boldsymbol{v} = \nabla\varphi$, and the phenomenon is governed by the Laplace equation for $\varphi$. Here, we consider an impermeable circular cylinder immersed within a main flow at speed $\boldsymbol{v}_0$. The velocity field is given by the superposition of the main stream velocity and the perturbation $\boldsymbol{v}'$ induced by the obstacle. The fundamental solution of the problem and its normal derivative on $\Gamma$ are

$$G(\boldsymbol{x},\boldsymbol{y}) = -\frac{1}{2\pi}\,\ln r, \quad \frac{\partial G}{\partial n} = -\frac{1}{2\pi}\,\frac{\boldsymbol{r}\cdot\boldsymbol{n}}{r^2}; \tag{15}$$

where $r = \|\boldsymbol{x} - \boldsymbol{y}\|$. The analytical solution $\varphi_a$ exists and has the form (in polar coordinates) $\varphi_a = v_0 r\left(1 + R^2/r^2\right) cos(\theta)$. Fig. 4 shows the comparison of the numerical solution of the present method, $\varphi$, with the analytical solution $\varphi_a$. The convergence of the global error $\epsilon$, defined as

$$\epsilon = \sqrt{\int_\Gamma \left\| \frac{\varphi - \varphi_a}{\varphi_a} \right\|^2 d\Gamma}, \tag{16}$$

is presented in Fig. 5 as a function of $1/N$ for different values of the the degree of the NURBS representation. Table 1 reports the values of the convergence rates measured using a linear regression of the error in the log-log plane, and the minimum error observed. What can be observed first, is that the

**Table 1.** Convergence rates for the solution of the Laplace equation.

| $p$ | Convergence rate | Error at $N$ max |
|---|---|---|
| 3 | 5.2850 | 1.88240447163443e-06 |
| 4 | 6.3204 | 1.98627799279891e-07 |
| 5 | 5.6809 | 5.88921480592586e-07 |
| 6 | 4.9574 | 3.86320539590748e-07 |

**Table 2.** Convergence rates for the scattering of a plane wave by a cylindrical obstacle.

| $p$ | Convergence rate | | Error at $N$ max | |
|---|---|---|---|---|
| | $f =$ 50 Hz | $f =$ 200 Hz | $f = 50$ Hz | $f = 200$ Hz |
| 2 | 4.0698 | 3.5075 | 0.000765660508167538 | 0.0444788053349804 |
| 3 | 5.2460 | 5.1965 | 0.000182807195261099 | 0.0149446263946068 |
| 4 | 7.4613 | 5.8926 | 2.02511544866008e-05 | 0.0051694130089412 |
| 5 | 8.4307 | 8.5100 | 1.02520999392619e-05 | 0.0016074909579270 |
| 6 | 9.2709 | 10.336 | 5.56624126228440e-06 | 0.0008186444737082 |

convergence curves are non linear in the log/log plane, and, consistently with the use of a rational function basis, the rate of convergence cannot be inferred directly from the order $p$ of the NURBS. The rate of convergence is slightly higher for lower $N$, gradually diminishes in finer simulations, and appears to be marginally dependent on the order $p$ of the NURBS. Indeed, the average rate is between $N^{-4}$ and $N^{-5}$ for $3 \leq p \leq 6$. Moreover, the best results are surprisingly obtained for $p = 4$. This phenomenon is not present in the acoustic simulations (see next section), and is currently under investigation. A possible reason could be related to the adoption of a uniform sampling in the NURBS parameter space which may produce unwanted oscillations of the higher-order functions.[8]

### 4.1.2. Scattering of a Planar Wave by a Circular Cylinder

In this case, the function $\varphi$ represents a physical quantity satisfying the wave equation in $\Omega$. The equation governing the propagation of an acoustic perturbation of angular frequency $\omega$ at speed $c_0$ is the Helmholtz equation, $\nabla^2\varphi + \kappa^2\,\varphi = 0$, where $\kappa = \omega/c_0^2$. Adopting the $e^{\mathrm{i}\omega t}$ time convention, the fundamental solution and its normal derivative on $\Gamma$ are

$$G(\boldsymbol{x}, \boldsymbol{y}, \kappa) = \frac{\mathrm{i}}{4}\,\mathcal{H}_0^{(2)}(\kappa\, r), \quad \frac{\partial G}{\partial n} = -\frac{\mathrm{i}\,\kappa}{4}\,\mathcal{H}_1^{(2)}(\kappa r)\frac{\boldsymbol{r}\cdot\boldsymbol{n}}{r}; \tag{17}$$

where $r = \|\boldsymbol{x} - \boldsymbol{y}\|$ and $\mathcal{H}_m^{(2)}(\kappa\, r)$ is the second-kind Hankel function of order $m$. The case study at hand consists of a plane wave of unit amplitude impinging on a circular cylinder of infinite length, for which the analytical solution is known (for example, see Morse and Ingard[15]). Indicating $\boldsymbol{\kappa}$ as the wave vector, the incident field is given by $\varphi_i = e^{i\,\boldsymbol{\kappa}\cdot\boldsymbol{r}}$. Figure 6 shows the solution at $f = 50$ Hz. The values of $|\varphi|$ at the solution points are indicated with squares, whereas the NURBS reconstruction of the solution along the whole boundary is depicted with the times sign. The agreement with the analytical solution is remarkable. The effect of the *h*-refinement can be observed in Fig. 7, where four knots have been inserted in the first and last intervals and two knots in the second and third ones. The refined solution is substantially indistinguishable from the analytical one. This excellent behavior is preserved also at higher frequencies, as Figs. 8, 9, and 10 show for $f = 200$ Hz, $f = 500$ Hz, and $f = 1000$ Hz, respectively.

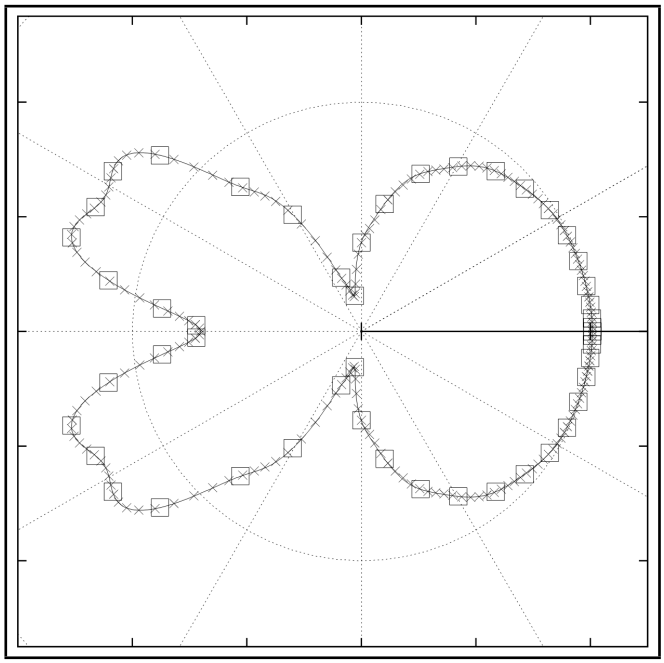

**Figure 9.** Scattering field at $f = 500Hz$, $(-)$ analytical, $(\times)$ BIE-NURBS, $(\square)$ BIE-NURBS at Greville's abscissae, $N = 50$, $p = 5$.

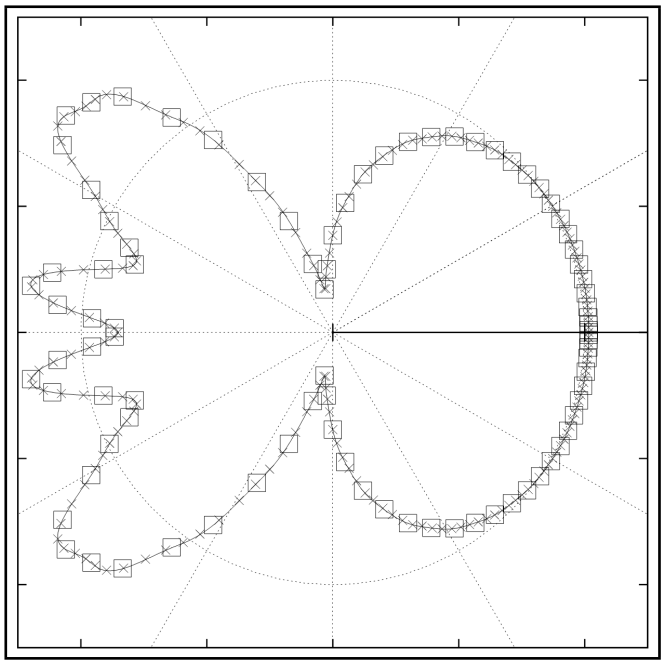

**Figure 10.** Scattering field at $f = 1kHz$, $(-)$ analytical, $(\times)$ BIE-NURBS, $(\square)$ BIE-NURBS at Greville's abscissae, $N = 90$, $p = 5$.

Also in this case, the convergence of the proposed formulation is evaluated using the global error $\epsilon$ defined in Eq. (16). The convergence analysis is performed using the *h*-refinement by inserting equally spaced knots. The convergence of $\epsilon$ as a function of $1/N$ is presented in Figs. 11 and 12 for $p = 2, 3, 4, 5, 6$ at $f = 50$ Hz and $f = 200$ Hz, respectively, whereas the convergence rates measured and the errors are reported in Table 2. As in the aerodynamic application, the log-log plots show a non-linear behavior. The major difference in the present application is in the progressive enhancement of the accuracy and rate of convergence as $p$ increases.

It can be observed that the rate of convergence is greater than

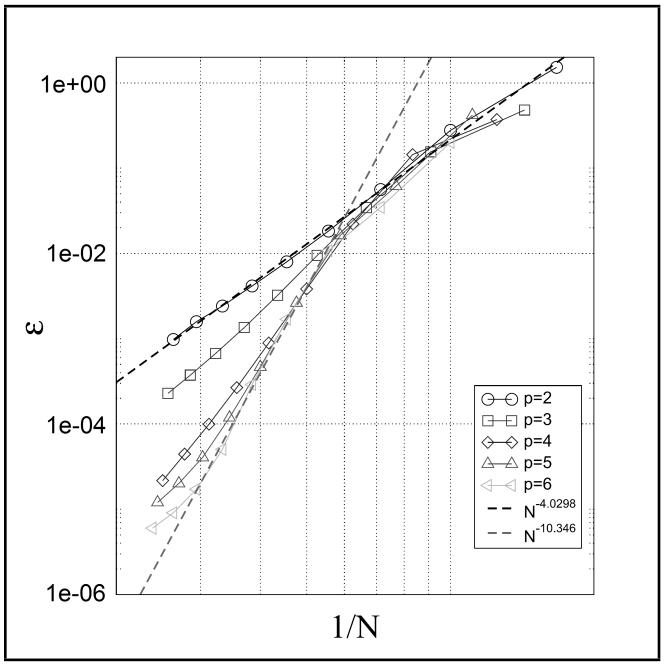


**Figure 11.** Convergence of $\epsilon$ at $f = 50Hz$.

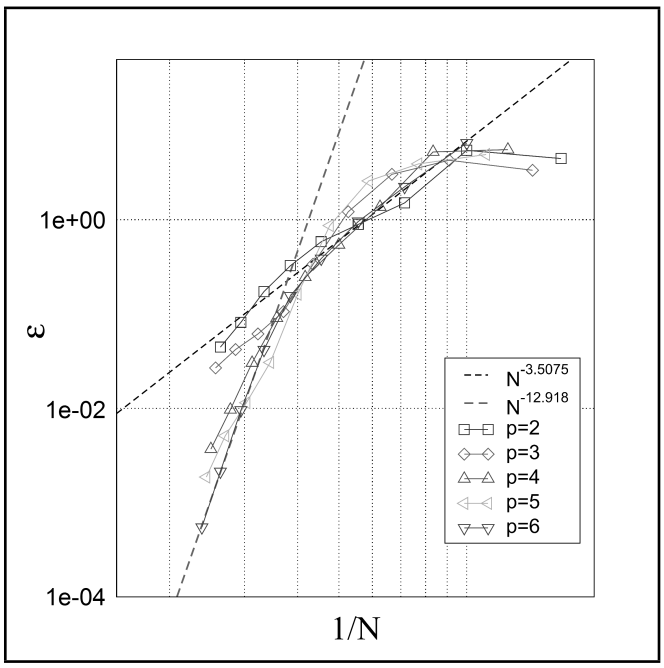


**Figure 12.** Convergence of $\epsilon$ at $f = 200Hz$.

$p$ for all the degrees tested, reaching values close to $\mathcal{O}(N^{-13})$ for $p = 6$ at the higher frequency, confirming the remarkable level of accuracy achievable with the *h*-refinement.

## 4.2. 2D Scattering of a Sound-Hard Quadrilateral Obstacle

After the assessment of the method by comparison with analytical results, it is worth testing its performance with a test case presenting features that can be critical for the global NURBS iso-geometric representation. It is the case of a geometry profile with corners, where the curvature becomes infinite, and where the NURBS could give meaningless results if not treated appropriately. The analyzed geometry is that of a cylinder with a square cross section, with side edge dimension $l = 2$. Figures 13 and 14 show the geometry of the cross section, as well as a close-up of one of the corner. In order to avoid the curvature singularity, there are two possible strategies. The first one is to divide the boundary profile into four macro-elements corresponding to the four edges of the square. This possibility falls in the same case analyzed in appendix A and is not repeated here. The second one relies on the elimination of the curvature singularity at the corner points by imposing a small, finite curvature radius $r_c$ (see Fig. 13). The global NURBS representation is directly applied to the approximated geometry so obtained, setting $r_c/l = 0.025$.

The solution of the present approach has been compared with the numerical solution obtained with the widely assessed commercial FEM software COMSOL.[16] The maximum ratio

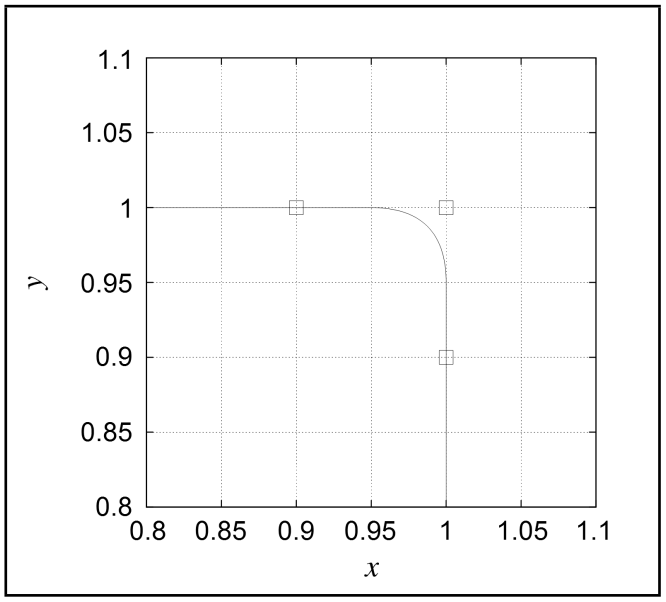


**Figure 13.** NURBS representation of the quadrilateral geometry. Markers indicate the control points used. The side dimension is $l = 2$, whereas the curvature radius $r_c$ of the approximated corner is such that $r_c/l = 0.025$.

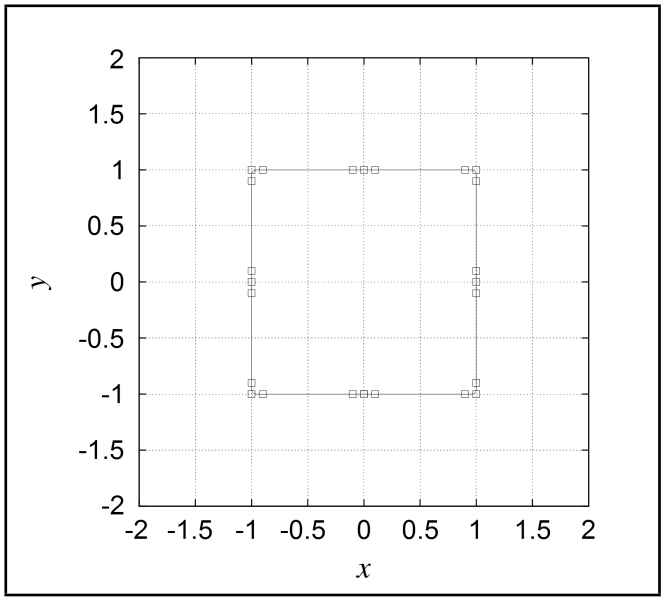


**Figure 14.** NURBS representation of the quadrilateral geometry. Close–up of the top right corner.

between the mesh element size and the wavelength has been set to $0.05$, in order to guarantee a converged reference solution with at least 20 elements per wavelength. The simulations of the present method are compared to the reference FEM solution in Figs. 15, 16 and 17. The first one depicts the absolute value of the scattered pressure on a circle of virtual microphones of radius $r_m = 20l$, whereas the second shows the total pressure along the upwind portion of the $x-$axis. In both cases, the frequency is $50$ Hz. The solution obtained with the proposed approach is in remarkable agreement with the FEM solution, revealing that the approximation of the corner points with a finite curvature profile does not significantly affect the numerical solution. It is important to stress that the integral coefficients were obtained here by numerical integration along the entire boundary, confirming that the global representation yields accurate results also for geometries with potentially critical features.

Figure 17 presents a direct qualitative comparison of the two fields obtained with the NURBS (left) and FEM (right) simulations. The absolute value of the total pressure obtained with the two methods is in remarkable agreement on all the domain portion analyzed.

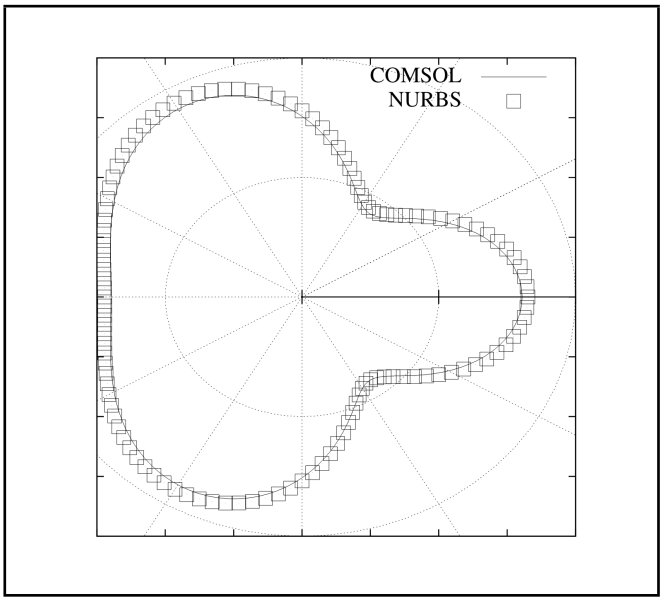


**Figure 15.** Scattered pressure evaluated at a circle of microphones with $r_m/l = 20$ (left) for $f = 50$ Hz. The continuous line indicates the FEM solution obtained with the COMSOL software.

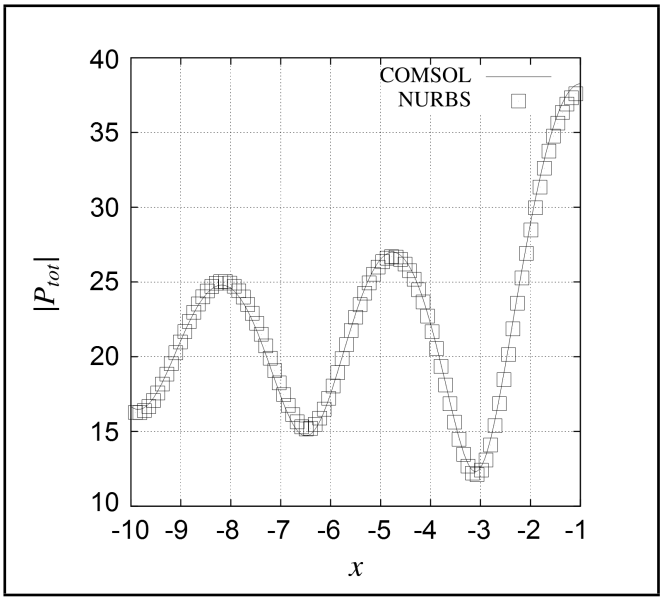


**Figure 16.** Total pressure evaluated along the upwind portion of the $x-$axis, for $f = 50$ Hz. The continuous line indicates the FEM solution obtained with the COMSOL software.

## 5. CONCLUDING REMARKS

A methodology for the numerical solution of BIE based on a global NURBS representation of dependent and independent variables has been presented. The non-local NURBS decomposition yields a meshless solution algorithm, which can be solved using a collocation method on the Greville abscissae in the NURBS parametric space. The unknowns of the resulting system of equations are the locations of the control points in the vector space the unknown function belongs to. The main advantage of the proposed methodology is the possibility to choose the order of the approximation at runtime, exploiting the recursive definition of the NURBS function basis. The method has been applied to problems of potential aerodynamics and acoustics for which analytical solutions are available. The preliminary results obtained reveal a remarkable agreement with the exact solutions. A very high convergence rate is achieved, reaching $\mathcal{O}(N^{-13})$ using sixth-order NURBS in the acoustic application. The reliability of the meshless isogeometric approach has been verified for geometries presenting critical features, such as corners and curvature changes. In all the test cases addressed, the global NURBS representation has revealed a very high accuracy and a substantial insensitivity to the extent of the numerical integration domain. The method is currently being extended to the analysis of three-dimensional problems, focusing on the treatment of the spurious eigenfrequencies affecting the numerical solution of exterior acoustics based on integral equations. Indeed, the peculiarities of the present approach observed and validated in the two-dimensional case suggest that the implementation of the classical regularization techniques, such as the CONDOR (Burton and Miller,[17]) or the CHIEF (Schenck,[18]), must be substantially revised to take advantage of the global NURBS representation. Specifically, a robust strategy to treat the hypersingular kernels arising in the Burton and Miller regularization is currently under analysis and will be the object of a future paper.

## REFERENCES

[1] Johnston, P. R. Second order Overhauser elements for boundary element analysis, *Mathematical and Computer Modelling*, **23** (5), 61–74, (1996).

[2] Camp, C. V. and Gipson, G. S. Overhauser elements in boundary element analysis, *Mathematical and Computer Modelling*, **15** (3), 59–69, (1991).

[3] Gennaretti, M., Giordani, A., and Morino, L. A third-order boundary element method for exterior acoustics with appli-

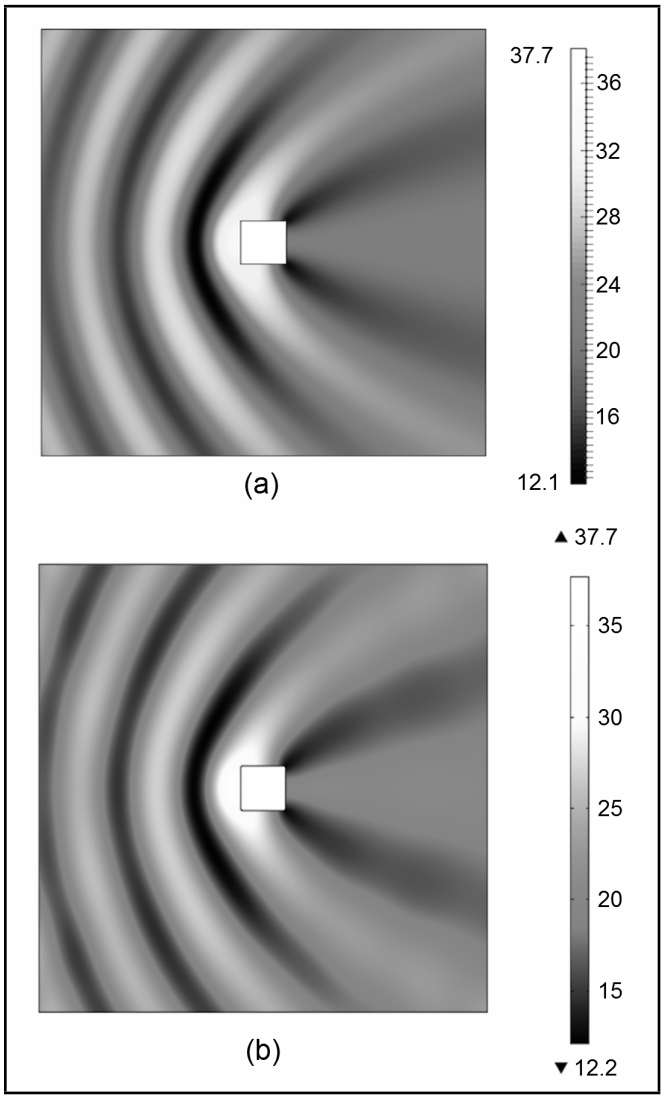


**Figure 17.** Absolute value of the total pressure field around the squared obstacle. The solution of the present method (a) is compared to the COMSOL FEM solution (b).

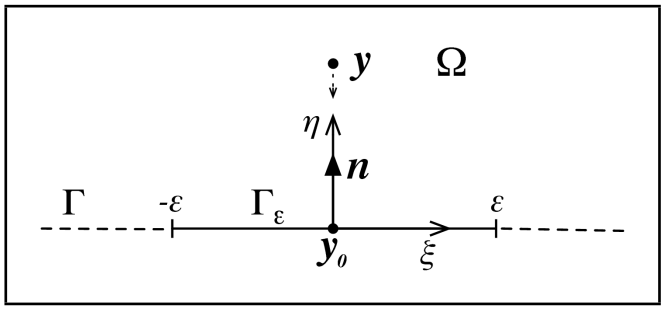


**Figure 18.** Observation point $\boldsymbol{y}$ approaching the boundary at $\boldsymbol{y}_0$.

cations to scattering by rigid and elastic shells, *Journal of Sound and Vibration*, **222** (5), 699–722, (1999).

[4] Iemma, U., Marchese, V., and Morino, L. High-order BEM for potential transonic flows, *Computational Mechanics*, **21** (3), 243–252, (1998).

[5] Iemma, U. and Burghignoli, L. A Hermite-Coons boundary element method, *Proc. 16th International Congress on Sound and Vibration, ICSV16*, Krakow, Poland, (2009).

[6] Morino, L., Iemma, U., and Cetta, F. Combining Hermite, Coons and Guyan: a highly efficient high-frequency finite element, In *Proc. 15th AIAA/CEAS Aeroacoustic Conference*, Miami, FL, USA, (2009).

[7] Rogers, D. F. *An Introduction to Nurbs: With Historical Perspective*, Morgan Kaufmann Series in Computer Graphics, Morgan Kaufmann Publishers, (2001).

[8] Piegl, L. On NURBS: a survey, *IEEE Computer Graphics and Applications*, **11** (1), 55–71, (1991).

[9] Simpson, R. N., Bordas, S. P. A., Trevelyan, J., and Rabczuk, T. A two-dimensional isogeometric boundary element method for elastostatic analysis, *Computer Methods in Applied Mechanics and Engineering*, **209-212**, 87–100, (2012).

[10] Kim, B. and Shin, Y. S. A NURBS panel method for three-dimensional radiation and diffraction problems, *Journal of Ship Research*, **47** (2), 177–186, (2003).

[11] Politis, C., Ginnis, A. I., Kaklis, P. D., Belibassakis, K., and Feurer, C. An isogeometric BEM for exterior potential-flow problems in the plane. *Proc. 2009 SIAM/ACM Joint Conference on Geometric and Physical Modeling*, 349–354, (2009).

[12] Hochstadt, H. *Integral Equations*, Wiley Classics Library, Wiley, (2011).

[13] Tricomi, F. G. *Integrals Equations*, Dover Books on Mathematics Series, Dover Publications, Incorporated, (1957).

[14] Johnson, R. W. Higher order b-spline collocation at the Greville abscissae, *Applied Numerical Mathematics*, **52** (1), 63–75, (2005).

[15] Morse, P. C. M. and Ingard, K. U. *Theoretical Acoustics*, International series in pure and applied physics, Princeton University Press, (1968).

[16] COMSOL Multiphysics, 1997-2008 COMSOL AB.

[17] Burton, A. J. and Miller, G. F. The application of integral equation methods to the numerical solution of some exterior boundary-value problems, *Proceedings of The Royal Society A*, **323**, 201–210, (1971).

[18] Schenck, H. A. Improved integral formulation for acoustic radiation problems, *Journal of the Acoustical Society of America*, **44** (1), 41–89, (1967)

[19] Kreyszig, E. *Advanced Engineering Mathematics*, John Wiley & Sons, (2010).

[20] Galassi, M., Davies, J., Theiler, J., Gough, B., Jungman, G., Alken, P., Booth, M., and Rossi, F. GNU Scientific Library—Reference Manual, Version 1.15. 2011. http://www.gnu.org/software/gsl/, (Accessed August 13, 2013).

**Table 3.** Real part of the double-layer integrals ($\times 10^3$) as a function of number of Gaussian abscissae $N_G$ and number of partition of the boundary $N_\Gamma$.

| **circle** | | | |
|---|---|---|---|
| | $N_G$=15 | $N_G$=30 | $N_G$=60 |
| $N_\Gamma$=1 | 5.13868867036 | 5.13868866829 | 5.13868867004 |
| $N_\Gamma$=2 | 5.13868867036 | 5.13868866829 | 5.13868867004 |
| $N_\Gamma$=4 | 5.13868867036 | 5.13868866829 | 5.13868867004 |
| **flower-like** | | | |
| $N_\Gamma$=1 | 8.567698577476 | 8.567693658759 | 8.567712281749 |
| $N_\Gamma$=2 | 8.567698577476 | 8.567693658759 | 8.567712281749 |
| $N_\Gamma$=4 | 8.567698577476 | 8.567693658759 | 8.567712281749 |

## APPENDIX A: KERNEL SINGULARITIES AND NUMERICAL INTEGRATION

The aim of the present section is to analyze the asymptotic behavior of the kernel $\mathcal{K}$ of Eq. (2) for $\boldsymbol{y} \to \boldsymbol{y}_0 \in \Gamma$ and its relationship with the strategy used for the numerical integration. The analysis deals with the two specific applications covered. Assume that the observation point $\boldsymbol{y}$ approaches $\Gamma$ from $\Omega$ (*i.e.*, from the positive side of the boundary) pointing to the boundary point $\boldsymbol{y}_o$ (see Fig. 18). The integral on the right hand side of Eq. (2) can be decomposed into two contributions: the integral over a straight segment $\Gamma_\varepsilon$ centered in $\boldsymbol{y}_o$ of length $2\varepsilon$, plus the integral over the remaining part of $\Gamma$

$$\mathcal{I}(\boldsymbol{y}) = \int_{\Gamma_\varepsilon} \varphi(\boldsymbol{x}) \frac{\partial G(\boldsymbol{y},\boldsymbol{x})}{\partial n}\, \mathrm{d}\Gamma + \int_{\Gamma\setminus\Gamma_\varepsilon} \varphi(\boldsymbol{x}) \frac{\partial G(\boldsymbol{y},\boldsymbol{x})}{\partial n}\, \mathrm{d}\Gamma. \tag{A.1}$$

Assuming $\varepsilon$ sufficiently small, $\mathcal{I}$ can be approximated as

$$\mathcal{I}(\boldsymbol{y}) \simeq \varphi(\boldsymbol{y}_o)\, \mathcal{I}^\varepsilon + \int_{\Gamma\setminus\Gamma_\varepsilon} \varphi(\boldsymbol{x}) \frac{\partial G(\boldsymbol{y},\boldsymbol{x})}{\partial n}\, \mathrm{d}\Gamma. \tag{A.2}$$

The kernels associated to the aerodynamic and the acoustic problems are

$$\begin{aligned} \mathcal{K}_{\mathsf{ae}}(\boldsymbol{x},\boldsymbol{y}) &= -\frac{1}{2\pi}\, \frac{\boldsymbol{r}\cdot\boldsymbol{n}}{r^2}, \\ \mathcal{K}_{\mathsf{ac}}(\boldsymbol{x},\boldsymbol{y}) &= -\frac{1}{4}\, \mathrm{i}\,\kappa\, \mathcal{H}_1^{(2)}(\kappa R)\, \frac{\boldsymbol{r}\cdot\boldsymbol{n}}{r}. \end{aligned} \tag{A.3}$$

Recalling the asymptotic form of $\mathcal{H}_1^{(2)}$ for small values of its argument (for example, see Kreyszig[19]), it can be easily seen that both $\mathcal{K}_{\mathsf{ae}}$ and $\mathcal{K}_{\mathsf{ac}}$ go to infinity as $r^{-1}$. Introducing the local coordinate $(\xi,\eta)$, such that $\boldsymbol{y} \equiv (0,\eta)$ and $\boldsymbol{x} \equiv (\xi,0)$ (see Fig. 13), it follows that

$$\mathcal{I}^\varepsilon_{\mathsf{ac}} = \int_{-\varepsilon}^{\varepsilon} \left[ \frac{-\eta}{2\pi\,(\xi^2+\eta^2)} + \mathrm{i}\,\eta \frac{\kappa^2}{16} \right] \mathrm{d}\xi = \mathcal{I}^\varepsilon_{\mathsf{ae}} + \frac{\mathrm{i}\varepsilon\kappa^2}{8}\,\eta. \tag{A.4}$$

It can be easily seen that

$$\mathcal{I}^\varepsilon_{\mathsf{ae}} = -\frac{1}{\pi} \arctan\frac{\varepsilon}{\eta}. \tag{A.5}$$

Taking the limit for $\boldsymbol{y} \to \boldsymbol{y}_0$ yields $\lim_{\eta\to 0} \mathcal{I}^\varepsilon_{\mathsf{ae}} = \lim_{\eta\to 0} \mathcal{I}^\varepsilon_{\mathsf{ac}} = -0.5$. Now, substituting the result into Eq. (A.2), it is possible to indefinitely shrink $\Gamma_\varepsilon$ to obtain for both acoustic and aerodynamics

$$\lim_{\varepsilon\to 0} \mathcal{I}(\boldsymbol{y}_0) = -\frac{1}{2}\, \varphi(\boldsymbol{y}_o) + \int_\Gamma \varphi(\boldsymbol{x}) \frac{\partial G(\boldsymbol{y},\boldsymbol{x})}{\partial n}\, \mathrm{d}\Gamma. \tag{A.6}$$

Substituting Eq. (A.6) into Eq. (2) follows that the domain function $E(\boldsymbol{y})$ equals 0.5 at a regular point $\boldsymbol{y}_0 \in \Gamma$. The remaining part of the integral (*i.e.*, the integral appearing in Eq. (A.6)) is a convergent improper integral and can be integrated using standard adaptive quadrature formulae capable of isolating the singularity of the integrand function.

In the present work, the Gauss-Kronrod adaptive quadrature rules have been used, as implemented in the GNU Scientific Library.[20] The results obtained are presented in Table 3, where the value of the real part of the integral in Eq. (A.6) is reported for different number of Gaussian integration points $N_G$. The influence of a partition of the boundary $\Gamma$ into $N_\Gamma$ parts has been also included. Two geometries have been analyzed: a circle and a flower-like geometry represented by the parametric equations $x(\theta) = [1+0.5\sin(5\theta)]\cos(\theta)$, $y(\theta) = [1+0.5\sin(5\theta)]\sin(\theta)$. As can be seen, the convergence of the integration is extremely fast, giving values substantially converged even with the coarsest quadrature rule. In addition, the partition of $\Gamma$ has no effects on the integral values, confirming the validity of the NURBS global representation for the meshless solution of the BIE. Needless to say, in presence of complex geometries, presenting slope and curvature discontinuities, the assumption of unit weights in Eq. (8) makes the accurate approximation of the integrand impossible, thus causing the numerical convergence of the quadrature rule impossible to be achieved when extended to the whole boundary. Nevertheless, in those specific cases the geometry can be partitioned into macro patches having the desired level of smoothness and the integrals in Eqs. (2) and (3) can be split into their restrictions to each continuous patch.